Available online at www.sciencedirect.com
SCIENCE DIRECT®
Optics Communications 227 (2003) 1–13
OPTICS COMMUNICATIONS
www.elsevier.com/locate/optcom

Extinction near-field optical microscopy

H.F. Hamann [a,b,*], M. Larbadi [a,1], S. Barzen [a], T. Brown [a], A. Gallagher [a,2], D.J. Nesbitt [a,2]

[a] JILA, University of Colorado, National Institute of Standards and Technology, Boulder, CO 80309-0440, USA
[b] IBM T.J. Watson Research Center, P.O. Box 218, Yorktown Heights, NY 10598, USA

Received 24 June 2003; accepted 7 August 2003

Abstract

This work presents a novel approach for apertureless, near-field scanning optical microscopy based on *extinction* of the incident beam for samples illuminated in evanescent fields and scanned with non-contact atomic force methods. The scheme exploits shot-noise limited detection of changes in reflected light intensity due to near-field interactions between the sample and a sharp atomic force microscope (AFM) tip as a function of probe–sample geometry, providing both high sensitivity (<0.1 ppm $Hz^{0.5}$) and absolute cross-section data for comparison with near-field model predictions. Extinction cross-section data for a Si probe in an evanescent field is measured as a function of excitation laser wavelength, which compare qualitatively well with Mie and Rayleigh theory for an effective ellipsoid model of the AFM tip. Extinction methods are then used to image single Au-nanoparticles (radius ≈ 7 nm), with the signal magnitudes interpreted via simple electrostatic near-field models for the probe–sample interaction.

1. Introduction

Prospects for nanoscale optical imaging far below the diffraction limit have triggered rapid development in near-field scanning optical microscopy (NSOM) methods in the last decade [1,2]. In aperture based NSOM, sub-diffractive imaging is typically obtained by near-field light leaking from the end of a tapered optical fiber and detected via absorption or fluorescence in the far-field [3–5]. Alternatively, in apertureless NSOM (ANSOM), one scans the enhanced near-field intensity near the tip of a sharp antenna-like nanoprobe and detects the scattering or fluorescence of the probe–sample interaction in the far-field [6–19]. One advantage of ANSOM is that spatial resolution is fundamentally limited only by tip size, which can be substantially below the diffraction limit ($\approx$1–5 nm) with standard fabrication technologies.

A major challenge for all high resolution NSOM methods has been the theoretical framework for inverting far-field signals to elucidate the near-field optical interaction between probe and sample. This has attracted considerable attention

* Corresponding author.
E-mail address: hendrikh@us.ibm.com (H.F. Hamann).
[1] Present address: Institute Nazionale per la Fiscia della Materia, Pisa, Italy.
[2] Staff Member, Quantum Physics Division, National Institute of Standards and Technology.

0030-4018/$ - see front matter
doi:10.1016/j.optcom.2003.08.039

from theory [20–33], which in turn requires quantitative experimental measurements of absorption, scattering, and extinction cross-sections of well-characterized samples. For *scattering* experiments, this proves particularly challenging, since only a small fraction of the far-field radiation is typically detected. As a result, a detailed knowledge of emission patterns from radiators at and near the surface of an interface (e.g., glass–air) is therefore necessary for quantitative interpretation. By way of contrast, *extinction* based methods, i.e., based on loss of photons from incident beam, offer a more directly interpretable measure of the probe–sample interactions. The focus of this work is to describe a novel extinction ANSOM method, based on scanning a vibrating, non-contact atomic force microscope (AFM) probe in the vicinity of a sample prism surface. Simply summarized, an incident laser beam illuminates an oscillating AFM cantilever probe and sample in a total internal reflection geometry, with the reflected power measured using lock-in detection at the oscillation frequency. The NSOM extinction signal (P_{ext}), i.e., diminution of reflected power by the probe and sample, is related to scattering and absorption by

$$P_{\text{ext}} = P_{\text{abs}} + P_{\text{scat}}, \tag{1}$$

where P_{abs} and P_{scat} are the absorbed and scattered power, and can be quantitatively compared to theories and recent studies of evanescent field scattering [8].

The organization of this paper is as follows. Section 2 describes key experimental details relevant to the extinction method. Section 3 presents results for extinction cross-section of a silicon probe in the evanescent field as a function of laser frequency, as well as imaging with this probe via the near-field interaction with 7 nm radius gold spheres. In each case, the observations are compared to predictions from simple theoretical models. Section 4 summarizes our conclusions.

2. Experiment

There are two basic parts to the apparatus shown in Fig. 1: an AFM and a prism with total-internal-reflection illumination. The entire apparatus is vibration isolated with springs down to a resonance frequency of ~0.8 Hz, with a laser beam focused at the prism surface. The weak extinction signal rides on much larger DC-signals, so the laser beam is amplitude stabilized and a low noise, subtractive optical detection scheme is used. The non-contact AFM operates via frequency feedback to maintain a constant height (z) above the surface, typically with 2–3 nm oscillation amplitude (A_{p} = peak amplitude). The oscillation is driven by a piezo slab between the tube piezo and the AFM probe.

The crucial requirement of such an extinction method is the ability to detect minute changes in the reflected far-field intensity. To achieve this, an amplitude-stabilized, p-polarized (along the probe axis) laser beam at 442, 488, 543, or 633 nm is focused with numerical aperture of ~0.20 onto the interior of a prism surface at 60° to the surface normal. The laser spot size is $\sim 3 \times 6\ \mu\text{m}^2$, limited by aberrations from focusing into the prism. The totally internally reflected laser beam is then collimated and measured by a "sample" Si photodiode, with a portion of the incident beam monitored with a second "reference" photodiode. The normalized signal from the reference photodiode is subtracted from that of the sample photodiode to reject common-mode noise, yielding extinction signal sensitivities at 500 nm of ~10 pW $\text{Hz}^{-0.5}$ for 0.1 mW laser power. This corresponds to a sensitivity of ~0.1 ppm $\text{Hz}^{0.5}$, within a factor of ~2 of the shot-noise limit. To maintain accurate subtraction of the light intensity, the gains of the two photodiode preamplifiers are matched via servo loop control (50 Hz bandwidth), feeding back on the DC signal level differences [34]. The resulting noise rejection is >60 dB at 300 KHz, for a total of 0.1–1.2 mW laser power on the photodiodes. The desired extinction signals are obtained by demodulating this difference at the cantilever frequency by dual phase lock-in detection with a typical bandwidth of 100 Hz.

These demodulated signals reflect the first derivative with respect to distance, $\text{d}P_{\text{ext}}(z)/\text{d}z$. In order to obtain absolute extinction signals, $P_{\text{ext}}(z)$, one must integrate $\text{d}P_{\text{ext}}(z)/\text{d}z$ from z out to the far-field ($z \gg \lambda$). To recover this integration

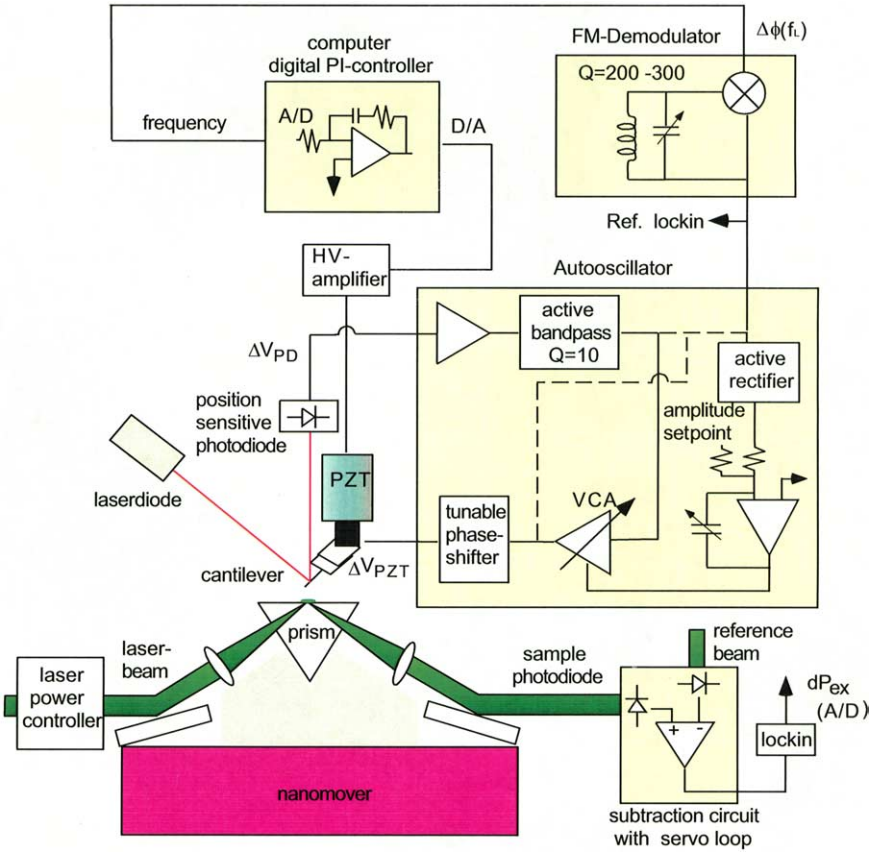

Fig. 1. Diagrammatic representation of the experimental apparatus. See text for details.

accurately requires small oscillation amplitudes ($A_p \sim 3$ nm) and thus careful design of the deflection electronics, specifically involving a low current noise source (<300 pA $Hz^{-0.5}$ @ 300 kHz) for the diode laser. For a well-matched 3mW spot on the lever arm, this results in near shot-noise limited performance (≈20 pA $Hz^{-0.5}$) and, neglecting contributions due to thermal noise, a theoretical S/N in excess of 65 dB $Hz^{0.5}$ [35].

The AFM feedback is realized using FM detection methods introduced by Albrecht et al. [36], based on probes with a resonant frequency of $f_L \approx 300$ kHz and quality factor $Q = 500$ [37]. As shown in Fig. 1, the output of the position-sensitive photodiode is filtered by a $Q = 10$ bandpass filter that rejects higher harmonics of the cantilever vibration. The oscillation amplitude, as monitored either by the piezo voltage (V_{PZ}) or the photodiode signal (V_{PD}),is stabilized by a fast, high-gain, amplitude-servo loop. In order to sustain oscillation, the amplitude is servo loop adjusted by a tunable phase-shifter to provide positive feedback.

This FM-detection method is particularly ideal for circumventing bandwidth limitations at high Q in vacuum applications. However, there are also several significant advantages for use under ambient pressure conditions, compared to conventional amplitude modulation (AM) methods of driving the lever off resonance and detecting changes in A_P due to variations in f_L. Most importantly, the FM-detection method can maintain a constant A_P with significantly larger bandwidths; this is especially useful when detecting scattered light modulation at f_L, because A_P is maintained *independently* of the AFM z-feedback. As a result, the FM approach is less sensitive to artifacts due

to insufficient stabilization of the tip vibration. Secondly, the FM method more easily yields A_P using the tip-vibration signal (V_{PD}, see Fig. 2) as a reference for lock-in. By way of contrast, phase-sensitive detection of the probe-scattered light using the drive signal (V_{PZ}) as a reference can be influenced by phase jitter between V_{PZ} and the lever motion (e.g., due to damping by a thin liquid layer on the surface, etc.). Finally, an additional advantage of FM-detection is that the measured frequency shifts (and therefore lever displacements) are not sensitive to amplitude noise or slow drift in the laser diode emission or deflection system.

The frequency of the cantilever auto oscillation is demodulated with a fast frequency (FM) detector, with a replica of the oscillation signal phase-shifted by a high Q (≈200–300) tunable bandpass filter. The phase-shifted auto oscillation and the original signal drive a mixer which monitors the frequency dependent phase-shift, achieving sensitivities up to 5 V/kHz with a noise floor of

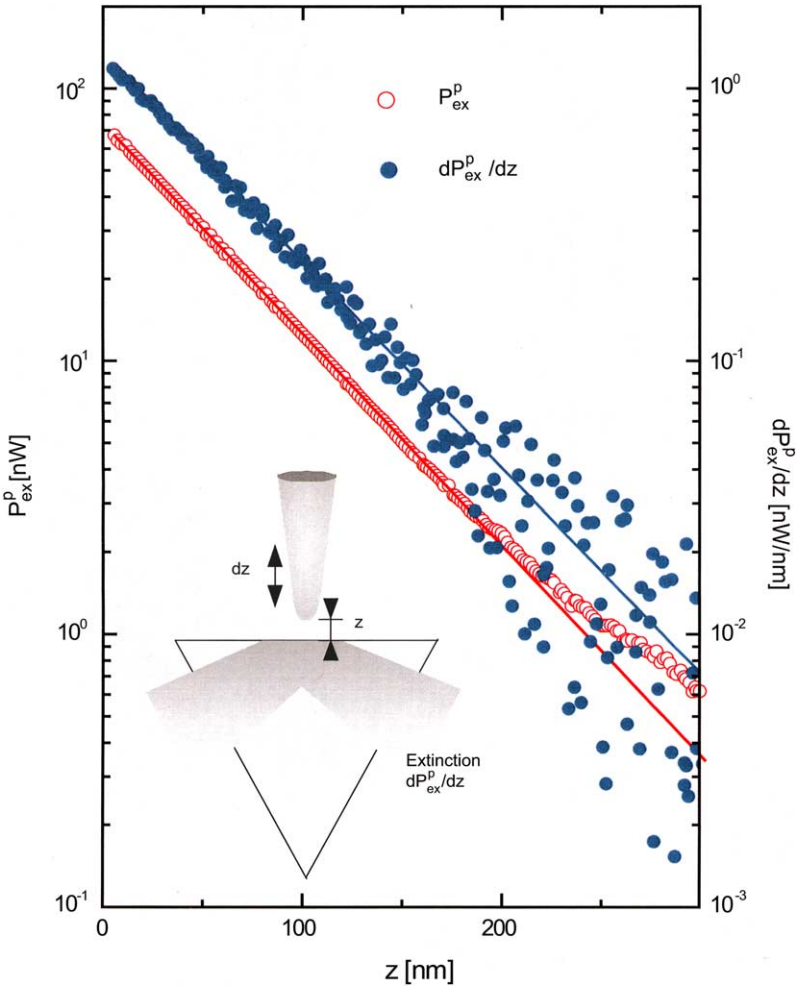

Fig. 2. Measured z-dependence of the fractional modulated extinction (solid circles) for a total internally reflected beam by an evanescently excited Si-probe at 543 nm. To obtain the DC extinction, the modulated extinction is integrated from z out to infinity (open circles). The solid lines are least-square exponential fits with 57 (2) nm and 56 (2) $1/e$ decay length for the differential and integrated extinctions, respectively.

<5 mHz/Hz$^{0.5}$ and in a bandwidth of $\approx$1.0 kHz (@ 300 kHz). The electronic noise of the FM-detector is well below the frequency noise of the cantilever ($\approx$1 Hz/Hz$^{0.5}$ @ 300 kHz, for $A_P = 3$ nm, $Q = 500$, and a spring constant of $\approx$50 N/m), which in turn is very close to the thermal noise limit at room temperature [36].

The oscillation-amplitude servo loop measures V_{PD} or V_{PZ} with an active full-wave rectifier, compares this with a set point in a summing amplifier, and sends the error signal to a voltage-controlled amplifier that drives the slab piezo. The choice of stabilizing on V_{PZ} or V_{PD} depends on the specific requirements in the extinction measurement, as well as the desired bandwidth. For imaging small surface regions, V_{PD} stabilization is the preferred method, because A_P is kept constant, independent of damping changes due to surface interactions. However, V_{PZ} stabilization is preferable for scanning larger ($>$100 nm) regions in our experiment setup, since the sensitivity of the deflection system changes slightly as the probe approaches the surface (i.e., $\approx$1%/100 nm). Consequently, V_{PZ} stabilization is more suitable to measure approach to the surface curves because then the sensitivity of the deflection system is not included in the servo loop and thus does not impact the extinction signals. Of course, the effective loop bandwidth achieved by these two amplitude stabilization schemes is quite different; V_{PZ} stabilization excludes, and V_{PD} stabilization includes, the high Q cantilever resonance. As a result, the bandwidth of the V_{PZ}-stabilization servo loop can be very high ($\approx$16 kHz), while the bandwidth in V_{PD} stabilization is limited only to f_L/Q (e.g., $\approx$600–1000 Hz).

3. Results and discussion

3.1. Extinction decay length and absolute cross-sections

First, we investigate extinction due to an evanescently excited Si-probe as a function of height (z) above the surface. Fig. 2 shows the modulated extinction amplitude, dP^{p}_{ext}/dz, versus height, $z = d + z_{st}$, where z_{st} is the AFM set point and d is the modulated tip displacement. In this notation, the superscript p refers to extinction purely by the probe, to differentiate from near-field contributions due to probe–sample interactions discussed later. To minimize PZT hysteresis effects, the data are taken while retracting and approaching the surface, with the results averaged. It is worth noting that dP^{P}_{ext}/dz (Fig. 2, right-hand axis) is in absolute units, which requires knowledge of the absolute modulation amplitude A_P. This was established by three independent methods: (i) calibrating V_{PD} vs probe–lever angle, and hence lever deflection, by displacing the photodiode by a known distance, (ii) interferometrically measuring the cantilever vibration amplitude (at f_L) versus V_{PZ}, (iii) comparing the ratio of modulated probe-scattering to total DC scattering signal as the probe penetrates the evanescent field. (The experimental arrangement of [6] was used.) All three methods yield consistent values for A_P within 3%. The absolute extinction values, $P^{P}_{ext}(z)$, (Fig. 2, left hand axis) are then obtained by integrating dP^{P}_{ext}/dz from z to ∞. The resulting extinction versus distance curves at the four experimental wavelengths are summarized in Fig. 3.

As clearly evident in these semilog plots (Figs. 2 and 3), both the modulated and integrated extinction values decay exponentially with distance. The z-dependent decay of an unperturbed evanescent field $I_{ev}(z)$ is given by

$$I_{ev}(z) = I^{0}_{ev} \cdot \exp(-2z/d_{ev}) \tag{2}$$

with $d_{ev} = (\lambda/n_2)/[2\pi(n_1/n_2 \sin(\theta))^2 - 1)^{0.5}]$, where I^{0}_{ev}, λ, n_1, n_2, and θ are the evanescent field intensity at $z = 0$, vacuum wavelength, refraction index of suprasil ($n_1 = 1.46$) and air ($n_2 = 1.0$) and incident angle ($\theta = 60°$), respectively. These predictions are in excellent agreement with experimentally measured $d_{ev}/2$ values (Table 1), which at first thought is a bit surprising, since the evanescent field is strongly perturbed by the probe tip. This quantitative level of agreement confirms that such near-field perturbations are highly localized and insufficient to skew the overall z-dependent drop off in the evanescent field. This is also consistent with a representative TEM image of the probe in Fig. 4, which clearly indicates a probe tip radius of curvature ($\approx$5 nm) of the much smaller than the evanescence decay length.

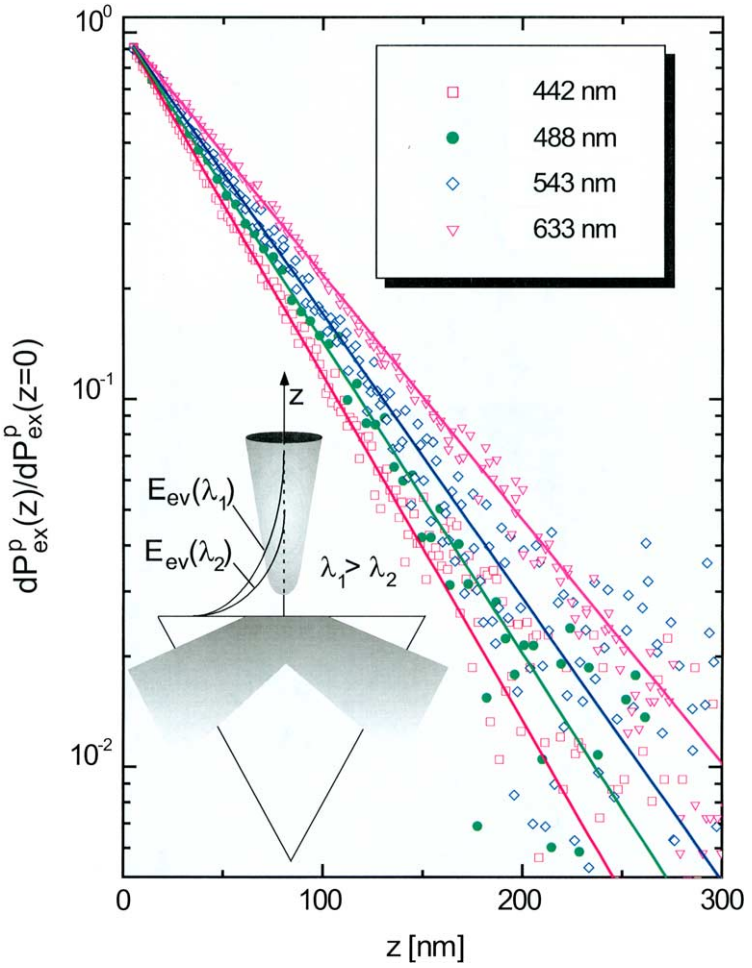

Fig. 3. Measured z-dependence of the fractional modulated extinction as a function of excitation wavelength, each normalized to unity for $z = 0$. The lines represent least-square exponential fits, with the decay constants reported in Table 1.

Table 1
Wavelength dependence of extinction cross-section for a single evanescently excited Si-probe

λ (nm)	dC^p_{ex}/dz (nm^2/nm)	$d_{ev}/2$ (nm)	Calc. $d_{ev}/2$ (nm)	C_{ex} (nm^2)
442	57(13)	46(2)	46.3	2630(715)
488	53(14)	50(1)	51.1	2660(755)
543	62(18)	57(1)	56.9	3500(1080)
633	71(17)	65(2)	66.3	4600(1243)

As a note of caution, these *extinction* based decay lengths should be compared to the corresponding d_{ev} values measured via *scattering* by the same shape Si probes [8]. Specifically, $d_{ev}/2$ was previously determined to be $\approx$70(3) nm for evanescent-field scattering at 543 nm, compared to $d_{ev}/2 \approx 57(1)$ nm from extinction based measurements. This significant difference can be attributed to strong changes in the angular scattering as a function of distance from the surface, e.g., a dipole

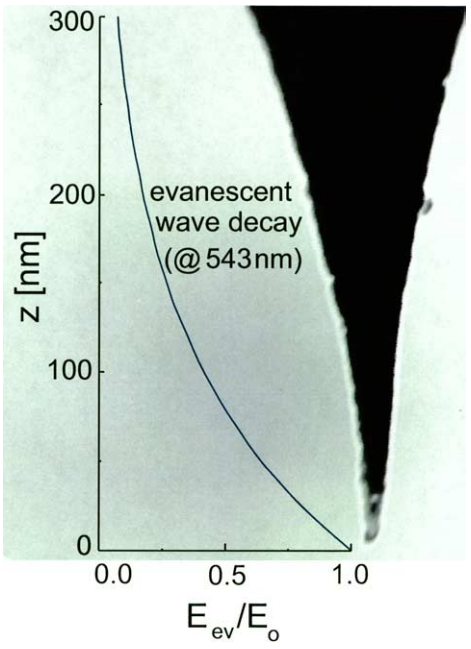

Fig. 4. TEM image of an Si AFM probe, at 408,000-fold magnification, with a superimposed distance scale for decay of the evanescent field. Such data are used for extracting volume parameters for the effective ellipsoid model analysis of the probe induced extinction studies.

at an air–quartz surface radiates preferentially (~80%) into denser medium, whereas this asymmetry disappears (~50%) several d_{ev} above the surface [38]. For any finite collection efficiency, therefore, scattering intensities will appear to drop off more slowly with distance. However, since all scattering contributes equivalently to loss of reflected power, the extinction method is completely insensitive to these angular effects.

After correction for differences in evanescent versus incident field strengths, the data in Fig. 2 can be further used to extract extinction cross-sections in *absolute* units. I^0_{ev} is related to the incident intensity I^0 by [39]

$$I^0_{ev} = \frac{4n_1^2\cos^2\theta}{\cos^2\theta + (\sin^2\theta - (n_2/n_1)^2)/(n_2/n_1)^4} I^0, \quad (3a)$$

$$I^0_{ev} = \frac{4n_1^2\cos^2\theta}{n_1^2 - n_2^2} I^0, \quad (3b)$$

for p-polarization and s-polarization, respectively. For the present experimental geometry and substrate, the incident intensities are therefore amplified at the air side of the quartz interface by 1.44- and 1.91-fold for p- and s-polarizations, respectively, with only a weak dependence on wavelength. As a more modest secondary effect, we also must determine the AFM setpoint, z_{set}, and therefore estimate the actual distance from the surface. To achieve this, we utilize force gradient results for a sphere over a flat surface with a Lennard–Jones pair potential, which predicts a cubic dependence of the frequency shift, i.e., $\Delta f = C/(z_{st} + d)^3$, where C is a known constant for a Si sphere (radius of 5 nm)-quartz interaction [40]. Fits to this expression for a fixed shift in frequency of $\Delta f \approx -300$ Hz yield an average set point distance $z_{st} = 5(3)$ nm, i.e., quite small compared to the observed z-dependence of the extinction curves.

To convert these extinction powers into intensities, the laser spot size is measured (in an independent experiment) by imaging fluorescence from a thin film of dye on the prism surface onto a CCD camera. The measured incident laser power and the laser spot size determine I^0 in Eqs. (3a) and (3b), from which the extinction cross-section $C^p_{ex} = P^p_{ex}(z = 0)/I^0_{ev}$ can be obtained. The resulting experimentally measured extinction cross-sections versus wavelength curves are summarized in Table 1, with values in the range of 2000–5000 nm^2. The uncertainties reported at a given wavelength reflect the distribution of extinctions observed for different probes from the same wafer.

As a further step toward interpreting the magnitude and wavelength dependence of these extinction cross-sections, we have explored simple analytical models based on Mie and Rayleigh scattering theory. It is worth noting that both Mie and Rayleigh theories are limited to finite objects in uniform electric fields, as opposed to the current situation of a semi-infinite, essentially conical object in an exponentially decaying evanescent field. However, since in the near-field electrostatic limit, the polarization is linearly proportional to the local E field, the *effective* volume that the probe experiences can be obtained by weighting each volume element by an electric field, i.e.,

$$V_{\text{eff}} = \int_0^\infty A(z)E_{\text{ev}}(z)/E_0\,\mathrm{d}z, \tag{4}$$

where $A(z)$ is the cross-sectional area of the probe and $E_{\text{ev}}(z)/E_0 = \exp(-z/d_{\text{ev}})$ is the evanescent-wave field at height z. More quantitatively, we have explicitly taken the z-dependent probe diameter directly from the TEM image (see Fig. 4), and integrated Eq. (4) numerically to extract V_{eff} as a function of excitation wavelength.

As a first approximation, we can equate this effective volume with a sphere of effective radius $a_{\text{eff}} = \sqrt[3]{3V_{\text{eff}}/4\pi}$. We then perform Mie calculations to determine the extinction cross-section for such an effective Si-sphere of this radius in a plane-wave field

$$C_{\text{ext}}^{\text{Mie}} = \frac{2\pi}{k^2}\sum_{n=1}^{\infty}(2n+1)\,\mathrm{Re}(a_n + b_n), \tag{5}$$

where a_n and b_n are the Mie coefficients [41] and the indices of refraction for crystalline Si are taken from [42]. These predicted cross-sections as a function of wavelength are compared (see Fig. 5) with the experimentally measured cross-sections, $C_{\text{ext}}^{\text{p}}$, where residual scatter in the experimental values (2σ of the mean) reflect slight differences in tip geometry from probe to probe. Fig. 5 demonstrates that Mie theory for an effective spherical object of the same volume qualitatively reproduces the magnitude and wavelength dependence of the measured $C_{\text{ext}}^{\text{p}}$ quite well. Quantitatively, however, the model systematically underestimates the actual extinction cross-sections at all wavelengths.

The reason that such a simple spherical model systematically *underestimates* the experimental extinction cross-sections in Fig. 5 is due to the prolate nature of the AFM probe. As a logical next step, therefore, we have calculated absorption and scattering cross-sections for ellipsoidally shaped particles in the Rayleigh limit, for which analytical solutions also exist. In this limit, the absorption and scattering cross-sections are given by

$$C_{\text{abs}}^{\text{Ray}} = k\cdot\mathrm{Im}(\alpha), \tag{6a}$$

$$C_{\text{scat}}^{\text{Ray}} = k^4\cdot|\alpha|^2/(6\cdot\pi), \tag{6b}$$

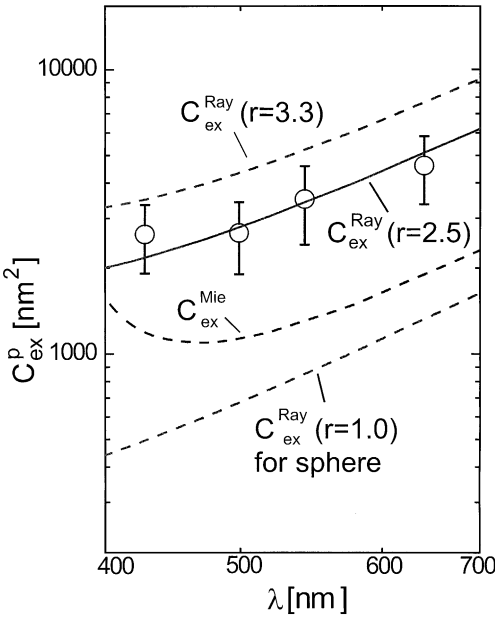

Fig. 5. Absolute extinction cross-sections for an evanescently excited Si AFM probe at the surface ($z = 0$) versus wavelength. Results vary by as much as 2-fold for different probes from a single wafer; average measurements are reported with error bars representing 2σ of the mean. Dashed lines represent various effective model results for (i) Mie scattering from Si spheres and (ii) Rayleigh scattering from Si ellipsoids of varying aspect ratios. Note the initially surprising, near quadratic *increase* in experimental cross-section at long wavelengths, and how this is well reproduced by both evanescent Rayleigh and Mie models. The solid line represents a best empirical fit to the data, based on Rayleigh scattering for an ellipsoid of $r = 2.5$.

where the polarizability is given by

$$\alpha = V_{\text{eff}}(\varepsilon - 1)/[1 + L(\varepsilon - 1)]. \tag{6c}$$

V is the effective particle volume, ε is the complex dielectric constant, and L is a function that depends analytically [43] on the aspect ratio, r, and the laser-polarization direction, $\hat{E}$. The magnitude of these elongation effects can be substantial; for example, Rayleigh scattering from a Si ellipsoid ($\varepsilon = 16.86 + 0.361\mathrm{i}$ at 543 nm) with an aspect ratio $r \approx 5$ (i.e., $L \approx 0.056$) is enhanced 11-fold over a sphere of the same volume. Indeed, in the limit of an *infinite* long spheroid ($r \to \infty$) of same volume and material, the absorption as well as scattering cross-section is increased by $\lfloor(\varepsilon_{\text{r}} + 2)^2 + \varepsilon_{\text{i}}^2\rfloor/9$, where ε_{r} is the real and ε_{i} is the imaginary part of ε. For example, for Si at 543 nm we find a maximum

possible increase in the cross-sections by as much as 40-fold.

The fact that the tip behaves like a prolate ellipsoid can be also immediately seen in polarization dependent extinction studies. Specifically, for p- versus s-polarization of the incident beam with respect to the prism surface, the extinction cross-section decreases by nearly an order of magnitude, from $dC^{p}_{ext}/dz = 62(18)$ nm^2/nm to $dC^{p}_{ext}/dz = 5.9(1.8)$ nm^2/nm, respectively. Cast into the context of a Rayleigh ellipsoid model, this ≈10:1 polarization dependence would correspond to an effective ellipsoid aspect ratio of $r \approx 3.3$ for the evanescently excited AFM probe.

This suggests the following analysis. For a given ellipsoid aspect ratio and a known $\varepsilon(\lambda)$, the wavelength dependence of dC^{P}_{ext}/dz in the Rayleigh regime can be readily calculated. These wavelength dependent results are summarized in Fig. 5 for two limiting cases: a sphere $(r = 1)$ and an ellipsoid $(r = 3.3)$, each with the same effective volume as used in the Mie calculations described above. The data of Fig. 5 indicate several trends worth noting. First of all, the strong dependence on ellipsoid aspect ratio is immediately evident, amounting to >5-fold increase in extinction cross-section at all wavelengths for the more prolate object. Second, the Rayleigh model correctly predicts an *increase* in extinction cross-section with wavelength. This is at first a bit surprising, since one well-known prediction of Rayleigh theory is a $C^{Ray}_{scat} \propto 1/\lambda^4$ dependence on wavelength, which would suggest a rapid *decrease* in extinction cross-section with increasing wavelength. The fundamental resolution of this paradox is that the evanescent decay length, d_{ev}, *increases* linearly with λ, resulting in a larger effective scattering volume. Specifically, as evident in Eq. (6a), there is an extremely rapid increase of extinction cross-section with effective particle size, (i.e., $C^{Ray}_{scat} \propto a^6_{eff}$), which with a $1/\lambda^4$ drop off in scattering cross-section predicts an overall quadratic dependence on wavelength.

The experimental results of Fig. 5 are in reasonable qualitative agreement with the predictions. Specifically, the cross-sections increase uniformly with wavelength, with a trend that is nearly quadratic (e.g., $a \approx 2$-fold observed increase for $a \approx 1.4$-fold increase in wavelength). The data fall between the two Rayleigh limits plotted in Fig. 5, suggesting an effective aspect ratio between $r = 1$ and $r = 3.3$. Indeed, the data can be empirically best fit for an effective aspect ratio of $r = 2.5$ $(L = 0.135)$, shown in Fig. 5. Given the sensitivity in these predicted extinction cross-sections to effective volume (and therefore tip shape, cone angle, etc.), this fit is well within experimental uncertainty due to variations between AFM probes. Alternatively summarized, these experimental data represent the first *absolute* cross-sections for extinction as a function of wavelength, the fundamental trends of which can be remarkably well reproduced by simple analytical scattering models, approaching nearly quantitative levels agreement with a single parameter to characterize the effective evanescent scattering geometry.

3.2. Extinction NSOM imaging: Au nanoparticles

With the absorption and scattering properties of the isolated probe adequately understood, we now demonstrate use of these extinction methods for near-field optical imaging of samples below the diffraction limit. Fundamentally, the potential for such NSOM imaging arises from the enhancement of the incident electric field in close proximity to the probe tip. Specifically, we look for the differential *increase* in extinction cross-section due to these near-field interactions between the probe and sample, as a function of scan coordinate.

By way of example, sample line scans are presented in Fig. 6 for extinction NSOM imaging at 543 nm of a gold (Au) nanoparticle (7 nm radius) and a Si probe. Fig. 6(a) (lower panel) shows data obtained during a non-contact AFM scan over a 7 nm Au particle at a frequency shift $\Delta f_L = -300$ Hz; this corresponds to a z-offset from the surface of $z_{set} \sim 5$ nm and the $z(x)$ topology (open circles). Fig. 6(b) (middle panel) presents raw data for the measured extinction signal, presented as *absolute* extinguished power per displacement of the probe (open triangles), for an incident power of ≈0.25 mW and an evanescent wave intensity of ≈20 μW/μm^2. Based on the measured probe displacement (i.e., $z(x)$) and the known z-dependence of the extinction curves (i.e., Fig. 5), one can also predict what these extinction signals would be in the

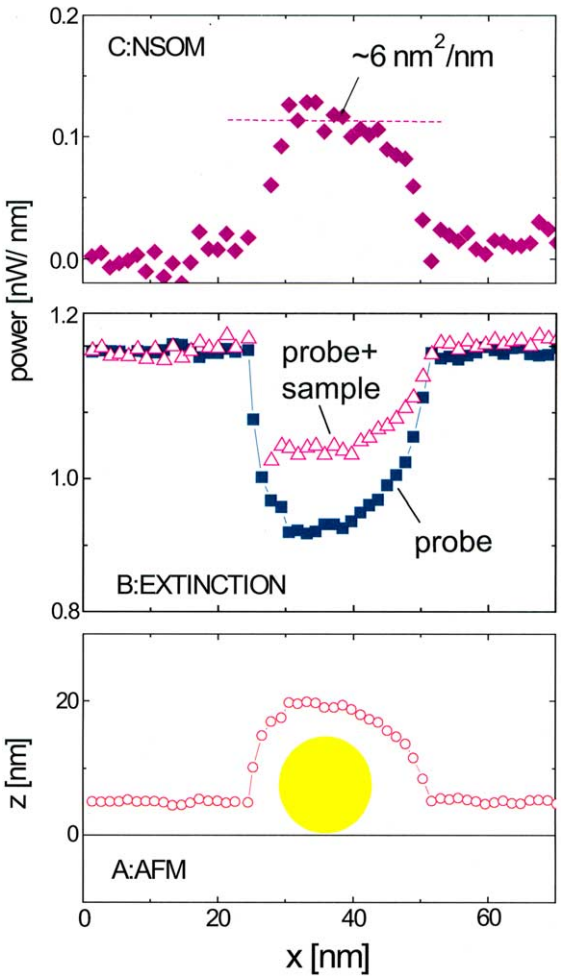

Fig. 6. Modulated extinction signal dP_{ext}^{p+s}/dz and topology data from AFM line scans over a single gold particle. (A) The bottom panel contains raw AFM data, establishing the trajectory of probe–prism height versus horizontal scan coordiante. (B) The middle panel shows the measured extinction signal dP_{ext}^{p+s}/dz, as well as the calculated signals dP_{ext}^{p}/dz for an equivalent $z(x)$ scan with the particle absent. The bottom panel presents the difference between these two signals, $(dP_{ext}^{p+s}/dz - dP_{ext}^{p}/dz)$, which represents the NSOM contribution to these extinction signals. In combination with the incident power (0.25 mW), which results into an evanescent wave intensity of $\sim$20 $\mu W/\mu m^2$ an extinction cross-section of $dC_{ext}^{NSOM}/dz \sim 6$ nm^2/nm can be obtained representing a sharp silicon tip interacting at 5 nm distance with a Au nanoparticle.

absence of the sample. Specifically, the dark squares in Fig. 6(b) are calculated from $dP_{ext}^{p}/dz = [dP_{ext}^{p}/dz]_0 \exp(-2(z(x))/d_{ev})$, where $[dP_{ext}^{p}/dz]_0$ is the extinction power far away from the nanoparticle at $z = 0$. The difference between the measured extinction curves with probe and sample (dP_{ext}^{p+s}/dz) and the extinction curve caused by the probe alone (dP_{ext}^{p}/dz) is therefore due to *near-field interactions* between the probe and sample, indicating an *increased* extinction in the presence of the nanoparticle. This excess extinction, $[dP_{ext}^{NSOM}/dz] = [dP_{ext}^{total}/dz] - [dP_{ext}^{p}/dz]$ is plotted in Fig. 6(c), and represents an alternative method for near field optical imaging with subdiffraction limited spatial resolution ($\ll \lambda$). By normalizing these powers to incident spot size, these data can be converted to *absolute* extinction cross-sections of $dC_{ext}^{NSOM}/dz \sim 6$ nm, for a silicon AFM tip ($\approx$12° cone angle) positioned over a Au nanoparticle (7 nm radius).

4. Discussion

To the best of our knowledge, the data in Fig. 6 represent the first *absolute* measurements of extinction due to the near-field effects for well characterized probe and sample geometries, which offers tantalizing prospects for a more rigorous comparison with exact near field theoretical calculations. As an initial contribution toward this goal, however, we briefly consider the following. The excess extinction signals represent a superpo-

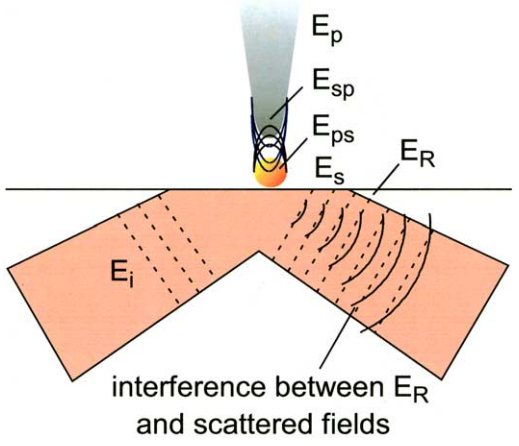

Fig. 7. The electric fields involved in extinction NSOM.

sition of all effects due to near-field probe + sample interactions (see Fig. 7). The relevant fields are (i) incident ($\mathbf{E}_i$), (ii) probe scattering ($\mathbf{E}_p$), (ii) sample scattering ($\mathbf{E}_s$), (iii) reflected ($\mathbf{E}_R$), (iv) sample scattering due to the near-field of the probe ($\mathbf{E}_{ps}$), and (v) probe scattering due to the near-field of the sample ($\mathbf{E}_{sp}$). To address the problem in a brief discussion, we consider a cylindrical probe–sample geometry with the probe directly above the sample, which permits the fields to be approximated by 1D complex scalars. As a final simplification, we treat the probe–sample interactions as a spheroid interacting with a sphere, where the evanescent field is taken to be constant over the spatial extent of the particles (as discussed in [44]).

In general, the experimentally monitored extinction is caused by destructive interference between the reflected field (phase advanced by 90° on total internal reflection) and the various scattering fields. Simple superposition considerations for the probe plus sample extinction thus yield

$$P_{\text{ext}}^{\text{p+s}}(z) = \left(1 - \left|\frac{E_R + E_s + E_p + E_{sp} + E_{ps}}{E_R}\right|^2\right) \times P_0 \exp\left(\frac{-2z}{d_{ev}}\right) \approx \left(2\text{Re}\left(\frac{E_p}{E_R}\right) + 2\text{Re}\left(\frac{E_{sp}}{E_R}\right) + 2\text{Re}\left(\frac{E_{ps}}{E_R}\right)\right) \cdot P_0 \exp\left(\frac{-2z}{d_{ev}}\right), \quad (8)$$

where the approximation in the second line is based on $E_R \approx E_p, E_{ps}, E_{sp}$, and neglecting $E_s \sim 0$, due to the small sample size. P_0 is the total power received by the detector, which matches the incident power. The first term of Eq. (8) represents the probe extinction $P_{\text{ext}}^{p}(z) \approx 2\text{Re}(E_P/E_R) \cdot P_0 \exp(-2z/d_{ev}) \approx C_{\text{ext}}^{p} \cdot P_0 \exp(-2z/d_{ev})/A_L$, which we have measured independently and discussed in detail above. Subtracting the probe extinction from Eq. (9) isolates the desired near-field contribution

$$P_{\text{ext}}^{\text{NSOM}}(z) = P_{\text{ext}}^{\text{p+s}}(z) - P_{\text{ext}}^{\text{p+s}}(z) \approx \left(2\,\text{Re}\left(\frac{E_{sp}}{E_R}\right) + 2\,\text{Re}\left(\frac{E_{ps}}{E_R}\right)\right) \times P_0 \exp\left(\frac{-2z}{d_{ev}}\right) \quad (9)$$

which is responsible for the peak NSOM extinction signal in Fig. 6. The terms in Eq. (9) represents the excess probe extinction due to the near-field of the sample and excess sample extinction due to the near-field of the probe, respectively. In the quasi-electrostatic limit, E_{sp} and E_{ps} are asymptotically phase delayed by $-\pi/2$ with respect to E_i and at a distance d given by

$$E \approx -k^2\,\text{Im}(\alpha\gamma)E_i/4\pi i d, \quad (10)$$

where k is the propagation constant ($k = 2\pi/\lambda$) and γ is the additional near electric field enhancement in the vicinity of the probe tip or sample. The reflected field is

$$E_R \approx -i\lambda E_i/\pi\,\text{NA}^2\,d, \quad (11)$$

where NA is the numerical aperture of the focusing lens. From Eqs. (9)–(11), the near-field contribution to the extinction signal at a distance z is therefore

$$P_{\text{ext}}^{\text{NSOM}}(z) \sim \frac{2\pi^2\,\text{NA}^2}{\lambda^3}(\text{Im}(\alpha_{sp}\gamma_s) + \text{Im}(\alpha_{ps}\gamma_p))P_0 \exp\left(\frac{-2z}{d_{ev}}\right), \quad (12)$$

where $\alpha_{sp}(\alpha_{ps})$ and $\gamma_p(\gamma_s)$ represent the near-field polarizability and enhancement, respectively, of the probe (sample) due to the near-field of the sample (probe).

Calculations of near-field polarizabilities and enhancements for a nearly conical probe tip geometry go substantially beyond the scope of the present work. However, near electric field enhancements due to such probe tips have been empirically obtained from previous work, whereby $|\gamma_p| \approx 10$ was estimated by measuring the near-field fluorescence *increase* for the probe tip positioned directly above dye impregnated nanoparticles [45]. This allows us to estimate the near-field polarizabilities for these tips, again in the simplifying context of an effective ellipsoid model for the probe. Specifically, from the analytic ellipsoid expression for $\gamma = \varepsilon/(1 + (\varepsilon - 1)L)$, with $\varepsilon = 16.86 + 0.361i$ for Si at 543 nm, a net probe field enhancement of $|\gamma_p| \approx 10(\gamma_p = 10.025 + 0.122i)$ corresponds to a depolarization factor of $L \sim 0.043$. Geometrically, such a value of L translates into a near-field aspect ratio of $r = 6.1$ for the probe tip, i.e., two to three times larger than empirically obtained from probe extinction measurements.

However, these previous measurements necessarily averaged over the full evanescent decay length, whereas the near electric field enhancement effects are in fact strongly localized around the probe tip ($\approx$5 nm), so a somewhat more prolate effective ellipsoid for such an analysis is not unreasonable. For the Au sample, we are back on solid analytical ground; exact expressions for a spherical Au particle ($L_s = 1/3$, $\varepsilon_s, = 5.396 + 2.228i$ [46]) predict a near-field enhancement of $\gamma_s = 4.24 + 0.81i$.

To predict the desired NSOM contributions to the extinction signals from Eq. (12), we need the near-field polarizabilities α_{ps} and α_{sp}, which for an ellipsoid model requires estimating the effective volumes (V_{eff}^{ps} and V_{eff}^{sp}) interacting with these enhanced near-fields for both probe and sample. In analogy with Section 3.1, we calculate these volumes geometrically, based on a dipolar falloff of these near-fields as $1/d^3$, and integrating over differential volume elements weighted by the appropriate sample or probe near electric field. As illustrated in Fig. 8, for calculating fields due to the sample, d is referenced to the center of the Au sphere, while for the probe, d is referenced to the center of a sphere embedded in the effective ellipsoid tip. The radius of probe tip end is assumed to be $r_p = 5$ nm. For a probe tip directly above the sample, with $z_{set} = 5$ nm, this integration procedure yields $V_{eff}^{ps} = 46$ nm^3 and $V_{eff}^{sp} = 697$ nm^3, which in conjunction with Eq. (6c), the appropriate depolarization factors L, and known dielectric constants for Si and Au at 543 nm yields near-field polarizabilities of $\alpha_{ps} = (221 + 55i)$ nm^3 and $\alpha_{sp} = (6580 + 89i)$ nm^3. With these calculated probe and sample values for α and γ, Eq. (12) can be used to predict absolute magnitudes for the expected NSOM extinction signals assuming an effective numerical aperture of $\approx$0.1. This yields $dC_{ext}^{NSOM}/dz \approx 10$ nm^2/nm for the tip 5 nm above the sample, i.e., already achieving qualitative agreement with experimental results in Fig. 6 of ≈ 6 nm^2/nm [47]. Indeed, these results provide strong encouragement for more rigorous theoretical calculations of NSOM extinction effects, which we hope the present absolute cross-section data for systems with well-characterized geometries will serve to stimulate.

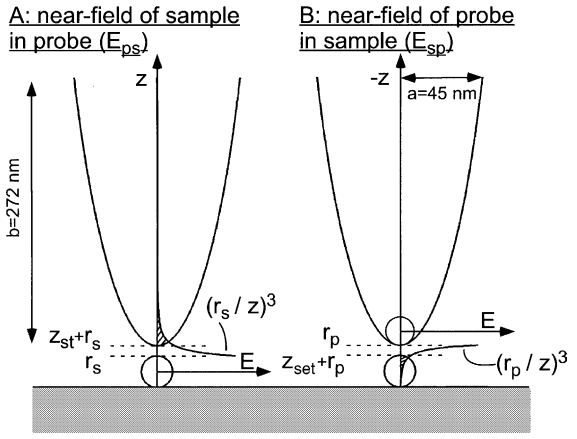

Fig. 8. The simple electrostatic model used to estimate NSOM extinction caused by near-field interactions between the sample and probe (drawn to scale).

5. Summary and conclusion

This work has focused on quantitative aspects of apertureless near-field optical microscopy. We have presented an alternative ANSOM method, based on extinction of modulated reflected light in a probe–sample system in an evanescent field. By virtue of shot noise limited detection on the reflected beam, sufficient optical sensitivity to small fractional intensity changes is obtained (<0.1 ppm Hz$^{0.5}$) with which to monitor these extinction effects with high enough S/N for imaging purposes. This extinction method offers particularly important advantages for quantitative near-field measurements. Specifically, since the reflected beam is collected with essentially 100% efficiency, the results are independent of assumptions about the far-field angular distribution of light scattered by the probe, and does not require careful alignment of the light-collection assembly onto the evanescent spot.

Measurements of extinction by an AFM probe in an evanescent field versus probe height yield exponential decay, with decay constants that agree quantitatively with expectations for an unperturbed evanescent field. Absolute extinction cross-sections are reported for an evanescently excited Si AFM probe of well characterized shape, as a function of wavelength and incident polarization.

These data have been analyzed in the context of analytical Mie and Rayleigh scattering models for effective spheres/ellipsoids, which correctly predict a quadratic *increase* of extinction cross-section with wavelength. Near-field interactions between a single Au-nanoparticle and a sharp AFM probe have been used to obtain high resolution NSOM images by monitoring far-field extinction in presence and absence of the sample. The absolute magnitudes of these NSOM extinction signals have been investigated with simple near-field models based on effective ellipsoids, and which provide promising levels of agreement with experiment.

Acknowledgements

This work has been supported by the National Institute of Standards and Technology as well as funds from the National Science Foundation.

References

[1] M.A. Paesler, P.J. Moyer, Near-Field Optics, Wiley, New York, 1996.
[2] S. Kawata, M. Ohtsu, M. Irie (Eds.), Nano-Optics, Springer, New York, 2002.
[3] D.W. Pohl, W. Denk, M. Lanz, Appl. Phys. Lett. 44 (1984) 651.
[4] A. Lewis, M. Isscacson, A. Haratounian, A. Murray, Ultramicroscopy 13 (1984) 227.
[5] E. Betzig, J.K. Trautman, T.D. Harris, J.S. Wiener, R.L. Kostelak, Science 251 (1991) 1468.
[6] F. Zenhausern, M.P. O'Boyle, H.K. Wickramasinghe, Appl. Phys. Lett. 65 (1994) 1623.
[7] Y. Inouye, S. Kawata, Opt. Lett. 19 (1994) 159.
[8] H.F. Hamann, A. Gallagher, D.J. Nesbitt, Appl. Phys. Lett. 73 (1998) 1469, on p. 1470 there is a typo; the total scattered power P_{probe} is 36 nW and not 3.6 nW.
[9] F. H'dhili, R. Bachelot, G. Lerondel, D. Barchiesi, P. Royer, Appl. Phys. Lett. 79 (2001) 4019.
[10] B. Knoll, F. Keilmann, Nature (London) 399 (1999) 134.
[11] H.F. Hamann, M. Kuno, A. Gallagher, D.J. Nesbitt, J. Chem. Phys. 8596 (2001) 114.
[12] M. Specht, J.D. Perdaring, W.M. Heckl, T.W. Hänsch, Phys. Rev. Lett. 68 (1991) 476.
[13] A.E. Kryukov, Y.-K. Kin, J.B. Ketterson, Appl. Phys. Lett. 82 (1997) 5411.
[14] S. Akamine, H. Kuwano, Appl. Phys. Lett. 68 (1985) 579.
[15] K. Fukuzawa, Y. Tanaka, Appl. Phys. Lett. 61 (1997) 168.
[16] M. Labardi, S. Patane, M. Allegrini, Appl. Phys. Lett. 77 (2000) 621.
[17] C. Hubert, J. Levy, Appl. Phys. Lett. 73 (1998) 3229.
[18] C.J. Hill, P.M. Bridger, G.S. Picus, T.C. McGill, Appl. Phys. Lett. 75 (1999) 4022.
[19] A. Naber, D. Molenda, U.C. Fischer, H.J. Maas, C. Hoppener, N. Lu, H. Fuchs, Phys. Rev. Lett. 89 (2002) 210801.
[20] J.A. Porto, R. Carminati, J.J. Greffet, J. Appl. Phys. 88 (2000) 4845.
[21] P.C. Chaumet, A. Rahmani, M. Nieto-Vesperinas, Phys. Rev. Lett. 88 (2002) 123601.
[22] M. Xiao, J. Opt. Soc. Am. A 14 (1997) 2977.
[23] (a) C. Girad, Appl. Opt. 31 (1992) 5380;
(b) C. Girad, A. Dereux, Phys. Rev. B 49 (1994) 11344.
[24] J.P. Fillard, M. Castagne, C. Prioleau, Appl. Opt. 34 (1995) 3737.
[25] G. v.Freymann, T. Schimmel, M. Wegner, Appl. Phys. A 66 (1998) S939.
[26] H. Furukawa, S. Kawata, Opt. Commun. 148 (1998) 221.
[27] D.A. Lapskin, V.I. Bdykin, V.S. Letokov, J. Mod. Opt. 45 (1998) 747.
[28] Y.C. Martin, H.F. Hamann, H.K. Wickramasinghe, J. Appl. Phys. 89 (2001) 5774.
[29] I.Sh. Averbukh, B.M. Chernobrod, O.A. Sedletsky, Y. Prior, Opt. Commun. 161 (1999) 156.
[30] A.V. Zayatas, Opt. Commun. 161 (1999) 156.
[31] (a) R. Wannemacher, M. Quinten, A. Pack, J. Microsc. 194 (1999) 260;
(b) M. Quinten, Appl. Phys. B 70 (2000) 579.
[32] J.T. Krug, E.J. Sanchez, X.S. Xie, Appl. Phys. Lett. 81 (2002) 3663.
[33] J.L. Bohn, D.J. Nesbitt, A. Gallagher, J. Opt. Soc. Am. A 18 (2001) 2998.
[34] P.C.D. Hobbs, Opt. Photon. News April (1991) 17.
[35] G. Meyer, N.M. Am, Appl. Phys. Lett. 53 (1988) 2400.
[36] T.R. Albrecht, P. Grütter, D. Horne, D. Rugar, J. Appl. Phys. 69 (1991) 668.
[37] The probes have been supplied by Nanoprobe, Wetzlar, Germany.
[38] W. Lukosz, R.E. Kunz, J. Opt. Soc. Am. 67 (1978) 1607, also 1615.
[39] A.J. Meixner et al., Appl. Opt. 34 (1994) 7995.
[40] D. Sarrid, Scanning Force Microscopy, Oxford University Press, New York, 1994.
[41] G. Mie, Ann. Phys. (Leipzig) 25 (1908) 377.
[42] D.F. Edwards in: E.D. Palik (Ed.), Handbook of Optical Constants, Academic Press, Orlando, 1985.
[43] C.F. Bohren, D.R. Huffman, Absorption and Scattering of Light by Small Particles, Wiley, New York, 1983.
[44] H.F. Hamann, Z. Phys. Chem. 215 (2001) 1025.
[45] H.F. Hamann, A. Gallagher, D.J. Nesbitt, Appl. Phys. Lett. 76 (2000) 1953.
[46] P.B. Johnson, R.W. Christy, Phys. Rev. B 6 (1972) 4370.
[47] $\lambda = 543$ nm, NA = 0.1, $L_s = 0.333$, $L_p = 0.043$, $\varepsilon_s = -5.396 + 2.228i$, $\varepsilon_p = 16.86 + 0.361i$, $a = 45$ nm, $b = 273$ nm, $r_p = 5$ nm, $r_s = 7$ nm and $z_{set} = 5$ nm, $P_0 = 250$ μW. We calculate $P_p \sim 80$ μW.